## Non-Spherical Pauli Forbidden States in Deformed Halo Nuclei: Impact on the ${}^{7}\text{Be} + p$ Resonant States in the Particle Rotor Model

Shin Watanabe\*
National Institute of Technology (KOSEN), Gifu College, Motosu 501-0495, Japan and
RIKEN Nishina Center, Wako 351-0198, Japan

### Antonio M. Moro

Departamento de Física Atómica, Molecular y Nuclear, Universidad de Sevilla, Apartado 1065, E-41080 Sevilla, Spain and Instituto Interuniversitario Carlos I de Física Teorica y Computacional (iC1), Apartado 1065, E-41080 Sevilla, Spain (Dated: June 10, 2024)

**Background:** An important aspect of reducing nuclear many-body problems to few-body models is the presence of Pauli forbidden (PF) states, which are excluded in fully antisymmetrized calculations. Insufficient treatments of PF states in deformed halo nuclei underscore the need for model refinement.

**Purpose:** We propose a new method utilizing Nilsson states as PF states in the orthogonality condition model, and investigate the impact of PF states on the properties of resonant states.

**Method:** We investigate the scattering states of  ${}^8B$  within the Particle Rotor Model (PRM) framework based on a deformed  ${}^7Be$  core and p two-body model. We compare several methods for eliminating PF states and test them with the experimental data.

**Results:** Our model successfully reproduces the experimental excitation function for elastic scattering cross section by properly eliminating PF states. The same calculation predicts the presence of a low-energy bump in the inelastic scattering excitation function, although its position is overestimated by about 1 MeV compared to experimental data.

**Conclusion:** This study extends the applicability of the PRM, offering a comprehensive approach for exploring structures and reactions of loosely bound nuclei like <sup>8</sup>B. Future integration with the continuum discretized coupled channels (CDCC) method promises to further advance the research.

## I. INTRODUCTION

Beyond the conventional picture of spherical halos, recent experiments have revealed the existence of deformed halo nuclei [1–5]. They are characterized not only by their extended neutron distributions but also by the deformation of their core. An accurate description of deformed halo nuclei is a frontier in modern nuclear physics, integrating state-of-the-art models to elucidate the complex interplay between a valence nucleon and a deformed core [6–11]. In the context of few-body models, the continuum discretized coupled channels (CDCC) method has been significantly developed [12–15]. Originally, CDCC was designed to describe reactions involving a deuteron and a target nucleus (T), based on the p+n+T threebody model. Recently, CDCC has been extended to include core excitation effects, leading to the extended version of CDCC (XCDCC) [16-20]. For example, XCDCC has been applied to  $^{11}{\rm Be}$  scattering in the  $^{10}{\rm Be}+n+T$  three-body model with  $^{10}{\rm Be}$  core excitation, revealing significant interference between the valence and core excitations in the breakup reactions [21–23]. These efforts to accurately represent many-body systems through fewbody models are a foundational task, enabling us to interpret complicated phenomena from a simple perspective.

When reducing many-body problems to few-body models, we often encounter the challenge of handling Pauli forbidden (PF) states, especially for deformed nuclei. The PF states are automatically excluded from the many-body wave function through antisymmetrization, yet they require deliberate exclusion in few-body approaches. The problem becomes more involved when considering deformation effects, such as in the Nilsson model [24, 25] or in the particle rotor model (PRM) [26– 28]. Consider  ${}^{8}\text{B}$  in a  ${}^{7}\text{Be} + p$  two-body model as an example. In the spherical shell model, the last proton occupies the  $0p_{3/2}$  orbital, which can accommodate up to four protons. Consequently, there is no need for special treatment to eliminate PF states as long as we consider p-wave states. However, when considering deformation, the  $0p_{3/2}$  orbital splits into the [110 1/2] and [101 3/2] Nilsson orbitals, which can accommodate up to two protons, respectively. Therefore, the [110 1/2] orbital becomes forbidden, as it is already filled by two protons in the deformed <sup>7</sup>Be core, necessitating careful treatment of PF states.

In this study, we focus on the refinement of the projectile wave function of deformed halo nuclei using the PRM for further applications within the XCDCC reaction framework. We demonstrate various treatments for excluding the PF states and investigate their impact on the resonant-state properties. Previous research presented a simple method to eliminate PF states in the deformed halo nucleus  $^{31}$ Ne =  $^{30}$ Ne + n [27, 28]. In these works, the PF states are obtained as bound states, and

<sup>\*</sup> s-watanabe@gifu-nct.ac.jp; This work was conducted during a sabbatical leave at the Departamento de Física Atómica, Molecular y Nuclear, Universidad de Sevilla.

eliminated after solving the Schrödinger equation. Due to its simplicity, this technique has been widely used in many studies [22, 29–31]. However, as will be shown later, we find that this method cannot be directly applied to  ${}^{8}B = {}^{7}Be + p$ , where the PF state emerges as a resonant state, complicating its exclusion. To overcome this limitation, we propose using the Nilsson model to represent PF states in the orthogonality condition model (OCM) [32–34]. This method enables us to exclude the PF states before solving the Schrödinger equation. This approach not only overcomes the limitations encountered in <sup>8</sup>B calculation but also offers the way for broader applications. Integrating the projectile wave functions calculated from this method with commonly used reaction frameworks, such as the XCDCC method (for breakup), and the distorted-wave Born approximation (DWBA) and the Adiabatic distorted-wave approximation (ADWA) [35] (for transfer reactions), could significantly improve our understanding and predictive capabilities in nuclear physics.

This paper is organized as follows. In Sec. II, we first explain the PRM framework without considering the PF states. This section is divided into three subsections, each explaining a different method for treating PF states. Section II A provides a brief review of the treatment outlined in Refs. [27, 28]. In Sec. II B, we show the standard OCM using spherical PF states for comparison. In Sec. II C, we propose a new method using deformed PF states in the OCM. Section III presents the results obtained from these different models. Finally, the paper concludes in Sec. IV.

### II. FORMULATION

We consider the scattering states of  ${}^{8}B = {}^{7}Be + p$  using the two-body Hamiltonian with core excitation defined as

$$H_1 = T_r + V(r, \boldsymbol{\xi}) + h_{\text{core}}(\boldsymbol{\xi}), \tag{1}$$

where r denotes the coordinate between proton and the core, and  $\xi$  is the internal coordinate of the core, i.e., direction of the symmetry axis of the deformed core. The operator  $T_r$  represents the kinetic energy and  $h_{\rm core}$  is the internal Hamiltonian, governing the degree of freedom of the core:  $(h_{\rm core} - \epsilon_I)\phi_I = 0$ , where  $\phi_I$  is the rotational wave function with the core spin I, and  $\epsilon_I$  is the corresponding eigenenergy. In this study, an effective potential V is assumed to be

$$V(\mathbf{r}, \boldsymbol{\xi}) = V_{\text{def}}(\mathbf{r}, \boldsymbol{\xi}) + V_{\ell s}(r)\boldsymbol{\ell} \cdot \boldsymbol{s} + V_{\text{Coul}}(r), \quad (2)$$

where  $V_{\rm def}$  is a deformed potential,  $V_{\ell s}$  is the spin-orbit interaction with the angular momentum  $\ell$  and proton spin s=1/2, and  $V_{\rm Coul}$  is the Coulomb interaction. For simplicity, both  $V_{\ell s}$  and  $V_{\rm Coul}$  are treated as spherical potentials.

The total wave function of the  ${}^{7}\text{Be} + p$  system,  $\Psi_{JM}$ ,

is expanded as

$$\Psi_{JM}(\mathbf{r}, \boldsymbol{\xi}) = \sum_{c} \frac{u_c(r)}{r} \Phi_{c, JM}(\hat{\mathbf{r}}, \boldsymbol{\xi})$$
 (3)

with

$$\Phi_{c,JM}(\hat{\boldsymbol{r}},\boldsymbol{\xi}) = [\mathcal{Y}_{\ell j}(\hat{\boldsymbol{r}}) \otimes \phi_I(\boldsymbol{\xi})]_{JM}, \tag{4}$$

where J and M denote the total angular momentum of the system and its z-component, respectively, j is the total angular momentum combining  $\ell$  and s. The function  $\Phi_{c,JM}$  is the direct product of the spin-angular function  $\mathcal{Y}_{\ell j}$  and the core wave function  $\phi_I$ , where c indicates the channel  $c = \{\ell j I\}$ , and  $u_c$  describes the relative motion between the proton and the core in the c channel. The radial wave functions  $u_c$  are obtained by solving the set of coupled-channel equations

$$[T_{r\ell} - \varepsilon_I]u_c(r) + \sum_{c'} V_{cc'}(r)u_{c'}(r) = 0$$
 (5)

under the appropriate boundary conditions. Here,  $T_{r\ell}$  denotes the kinetic energy,  $V_{cc'}(r) = \langle \Phi_{c,JM} | V | \Phi_{c',JM} \rangle$  is the coupling potential, and  $\varepsilon_I$  is the relative energy defined as  $\varepsilon_I = \varepsilon - \epsilon_I$ , with  $\varepsilon$  being the total energy.

At this stage, the presence of PF states is not taken into account.

## A. Model I: Standard PRM

A simple method to eliminate the forbidden states in deformed halo nuclei is outlined in Refs. [27, 28]. We refer to this method as the "standard PRM (std-PRM)" to distinguish it from the models described later. First, we introduce the Nilsson Hamiltonian by omitting  $h_{\rm core}$  from Eq. (1) as

$$H_{\text{Nil}} = T_r + V(r, \boldsymbol{\xi}). \tag{6}$$

By solving the Schrödinger equation with  $H_{Nil}$ , using the same form of wave functions [Eq. (3)], we can conduct Nilsson model calculations within the PRM framework. In this calculation, several states with different J values, but having the same value of  $\Omega$ , become energetically degenerate if the model space  $\{\ell jI\}$  is sufficiently large. Here,  $\Omega$  denotes the projection of the total angular momentum onto the z' axis in the body-fixed frame. The anticipated behavior is schematically illustrated in Fig. 1(a), in which the deformation parameter  $\beta_2$  varies from 0 to a specific value  $\bar{\beta}_2$ . Note that each Nilsson orbital is doubly degenerate due to time-reversal symmetry. Following the standard procedure, we allocate two protons to each Nilsson orbital starting from the lowest energy level, enabling us to identify the Nilsson orbital that accommodates the last unpaired proton. Consequently, the  $[000 \ 1/2]$  and  $[110 \ 1/2]$  Nilsson orbitals are considered as the PF states. In Fig. 1, PF states are represented by

the filled circles, while the last proton is indicated by the open circle for further explanation.

Subsequently, by gradually increasing the value of core excitation energies to the physical ones, we can track the evolution of the Nilsson states. For convenience, we introduce  $\alpha h_{\rm core}$  to  $H_{\rm Nil}$ , where  $\alpha=0$  corresponds to the Nilsson model and  $\alpha=1$  denotes the PRM. This evolution is shown in Fig. 1(b). At this stage,  $\Omega$  is no longer a good quantum number, and each Nilsson orbital split into two states. Through this process, we can identify the states originating from the  $[000\ 1/2]$  and  $[110\ 1/2]$  Nilsson orbitals. These states, indicated as "(I) std-PRM" in Fig. 1(b), are interpreted as PF states, and subsequently excluded after solving the Schrödinger equation with  $H_1$ . The next lowest-energy state, shown by the open circle in Fig. 1(b), is then considered as the lowest-energy state in Model I.

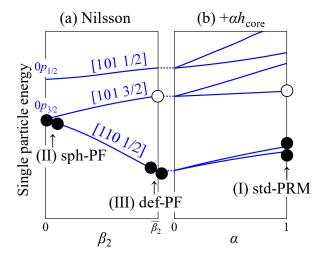


FIG. 1. Schematic illustration of the evolution of the single particle energy by incorporating (a) deformation and (b) core excitation. Panel (a) corresponds to the Nilsson diagram, where the deformation parameter  $\beta_2$  increases from 0 to a specific value  $\bar{\beta}_2$ . Panel (b) demonstrates the energy splitting by adding  $\alpha h_{\rm core}$  to  $H_{\rm Nil}$ , where  $\alpha=0$  corresponds to the Nilsson model and  $\alpha=1$  represents the PRM. The filled circles denote the PF states while the open circle indicates the last proton. Arrows labeled (I) std-PRM (standard PRM), (II) sph-PF (spherical PF states), and (III) def-PF (deformed PF states) are shown to explain various treatments of PF states. See text in detail.

## B. Model II: Spherical PF model

Another way of eliminating PF states is to introduce a Pauli blocking operator to Eq. (1), which is known as the orthogonality condition model (OCM) [32–34]. The Hamiltonian is defined as

$$H_2 = T + V + h_{\text{core}} + V_{\text{PF}} \tag{7}$$

with

$$V_{\rm PF} = \sum_{i=1}^{N_{\rm PF}} \lambda_i |\bar{\Psi}^{(i)}\rangle \langle \bar{\Psi}^{(i)}|, \qquad (8)$$

where the operator form is adopted for notational simplicity. In Eq. (8),  $\bar{\Psi}^{(i)}$  represents the *i*th PF state and  $N_{\rm PF}$  is the total number of PF states. In practice,  $\lambda_i = 10^6$  MeV is chosen to ensure convergence.

In the standard OCM, spherical PF (sph-PF) states are used to define  $\bar{\Psi}^{(i)}$  in Eq. (8). Therefore, in addition to our proposed model using the deformed PF (def-PF) states shown in the next subsection, we also conduct calculations using the sph-PF states. These sph-PF states (for given J and M) can be explicitly defined using the same form as Eq. (3):

$$\bar{\Psi}_{JM}^{(i)}(\boldsymbol{r},\boldsymbol{\xi}) = \sum_{c} \frac{g_c^{(i)}(r)}{r} \Phi_{c,JM}(\hat{\boldsymbol{r}},\boldsymbol{\xi}), \tag{9}$$

where  $g_c^{(i)}$  is the radial wave function. Once  $\bar{\Psi}_{JM}^{(i)}$  is determined, the set of coupled-channel equations for  $u_c$  is derived as follows:

$$[T_{r\ell} - \varepsilon_I] u_c(r) + \sum_{c'} V_{cc'}(r) u_{c'}(r) + \sum_{c'} \int dr' W_{cc'}(r, r') u_{c'}(r') = 0,$$
 (10)

where  $W_{cc'}(r,r')$  is the non-local potential defined as

$$W_{cc'}(r,r') = \sum_{i=1}^{N_{PF}} \lambda_i g_c^{(i)}(r) g_{c'}^{(i)*}(r').$$
 (11)

These non-local coupled-channel equations are solved under the same boundary condition as for Eq. (5). The R-matrix code available in Refs. [36, 37] is utilized.

In the actual  ${}^7\mathrm{Be} + p$  calculation of the sph-PF model, the sph-PF states, equivalent to two  $0p_{3/2}$  states, are determined in the Nilsson model by setting  $\beta_2 = 0.0001$  instead of zero. This minimal  $\beta_2$  is necessary to avoid possible configuration mixing of the four  $0p_{3/2}$  states, which could occur at  $\beta_2 = 0$  due to the degeneracy of  $\epsilon_I = 0$ , as described by  $[\mathcal{Y}_{p3/2} \otimes \phi_I]_{JM}$ . Introducing a small  $\beta_2$  value effectively resolves this degeneracy and aligns the states, allowing for a reasonable definition of sph-PF states corresponding to two [110 1/2] Nilsson states in the spherical limit. These well-defined states are then employed as the PF states in Eq. (8), which are indicated as "(II) sph-PF" in Fig. 1.

## C. Model III: Deformed PF model

As a novel approach, we propose using def-PF states in the OCM, which we call the def-PF model. In this model, we assume that  $\bar{\Psi}^{(i)}$  in Eq. (8) should be deformed rather

than spherical. A natural choice is to use the ith Nilsson state, which is indicated by "(III) def-PF" in Fig. 1. As discussed in Sec. II A, the Nilsson state (for given J and M) can be obtained by solving the Schrödinger equation with  $H_{\rm Nil}$  within the PRM framework. Therefore, the Nilsson states  $\bar{\Psi}_{JM}^{(i)}(r,\boldsymbol{\xi}) \equiv \langle JM;r,\boldsymbol{\xi}|\bar{\Psi}^{(i)}\rangle$  are explicitly defined in Eq. (9). Once  $\bar{\Psi}_{JM}^{(i)}$  is determined, the set of coupled-channel equations (10) is solved in the same way as described in Sec. II B.

### III. RESULTS

## A. Model Setting and Structure Analysis

In the actual calculation, we start with the potential parameters for the spherical model shown in Ref. [38]. For simplicity, the core-spin orbit interaction, i.e.,  $V_{LI}$  in Ref. [38], is neglected. For the deformed potential  $V_{\text{def}}$ , we adopt the deformed Woods-Saxon potential with radius  $R_0 = 2.391$  fm and diffuseness  $a_0 = 0.535$  fm. The depth of this deformed Woods-Saxon potential, denoted as  $V_{\text{def}}^0$ , will be determined later. The Woods-Saxon volume type is employed for  $V_{\ell s}$ , with a depth  $V_{LS}^0 = -7$ MeV, and the same radius  $R_0 = 2.391$  fm and diffuseness  $a_0 = 0.535$  fm. Regarding the core state, we consider the states from I = 1/2 to 13/2 to clearly define the PF states. For the energies  $\epsilon_I$  corresponding to these states, we use the experimental data for the four lowest-energy states ( $\epsilon_{3/2} = 0 \text{ MeV}$ ,  $\epsilon_{1/2} = 0.43 \text{ MeV}$ ,  $\epsilon_{7/2} = 4.57 \text{ MeV}$ , and  $\epsilon_{5/2} = 6.73$  MeV). For the higher-energy states, we use extrapolated values using the formula [39, 40]:

$$\epsilon_I = \epsilon^0 + A \left[ I(I+1) + a(-)^{I+1/2} (I+1/2) \right],$$
 (12)

where the constants ( $\epsilon^0$ , A, and a) are determined from the three lowest experimental energies:  $\epsilon^0 = -0.564$  MeV, A = 0.486 MeV, and the decoupling factor a = -1.29. The deformation parameter  $\beta_2$  is set to 0.586.

First, we solve the Schrödinger equation using  $H_{Nil}$ to define the PF states. Figure 2(a) presents the Nilsson diagram obtained within the PRM framework. The resonant energies indicated by the dotted lines are estimated using the complex scaling method [41, 42]. In the standard Nilsson model [24, 25], each orbital is doubly degenerate. In contrast, in our calculations, the number of Nilsson states depends on  $J^{\pi}$  and the model space  $\{\ell jI\}$ . For example, for  $J^{\pi}=0^+$ , only one state is obtained for the  $[110 \ 1/2]$  Nilsson orbital because only the  $[\mathcal{Y}_{p3/2} \otimes \phi_{3/2}]_{0+}$  configuration is allowed with  $p_{3/2}$ . Note that the energies corresponding to a specific Nilsson orbital are degenerate for different  $J^{\pi}$ . This degeneracy allows us to identify which state corresponds to which Nilsson orbital. Consequently, states up to the [110 1/2] orbital are considered as the PF states in Model III. For the negative-parity states  $(J^{\pi} = 1^{-} \text{ and } 2^{-})$ , the [000] 1/2] Nilsson states are regarded as the PF states.

On the other hand, in Model I, we further trace how the Nilsson states evolve by adding  $\alpha h_{\rm core}$  to  $H_{\rm Nil}$ . In Fig. 2, panels (b) to (e) illustrate the energy splitting for  $J^{\pi}=0^+$  to  $3^+$ , respectively. This procedure enables us to identify the states originating from the [110 1/2] Nilsson orbital, which are considered to be PF states. Subsequently, the PF states are extracted after solving the Schrödinger equation with  $H_1$ . However, for the  $J^{\pi}=3^+$  state, one of the PF states significantly increases in energy and approaches the next energy level in the continuum region. This situation makes it difficult to unambiguously identify the PF state from the solution. We therefore show the results without excluding this PF state in Model I.

Next, we determine the potential depth  $V_{\text{def}}^0$  for each  $J^{\pi}$  configuration through the following procedure. For the  $J^{\pi}=2^{+}$ ,  $1^{+}$ , and  $3^{+}$  states,  $V_{\text{def}}^{0}$  is adjusted to the experimentally well-established bound and resonant energies:  $\varepsilon_{gs}(2_1^+) = -0.137 \,\text{MeV} (E_x = 0 \,\text{MeV}), \, \varepsilon_{res}(1_1^+) =$ 0.63 MeV ( $E_x = 0.77 \text{ MeV}$ ), and  $\varepsilon_{\text{res}}(3_1^+) = 2.18 \text{ MeV}$  $(E_x = 2.32 \text{ MeV})$ . As for the 3<sup>+</sup> states in Model I, we assume that the  $3_1^+$  state corresponds to the PF state and that the  $3^+_2$  state is the physical one, which is adjusted to the experimental data. For the  $J^{\pi}=0^+, 1^-, \text{ and } 2^$ states,  $V_{\text{def}}^{\hat{0}}$  is tuned so as to reproduce the phase shift calculated by the ab initio no-core shell model/resonating group method (NCSM/RGM) [10]. In Fig. 3, panels (a)  $J^{\pi} = 0^{+}$ , (b)  $J^{\pi} = 1^{-}$ , and (c)  $J^{\pi} = 2^{-}$  display the resultant phase shifts. The solid lines represent the results of the def-PF model, which fairly reproduce the NCSM/RGM calculations shown by the dashed lines. Note that the results of the std-PRM are almost identical. The determined  $V_{\text{def}}^0$  values are summarized in Table I. It is interesting to note that the obtained parameters remain almost constant for all  $J^{\pi}$  states, contrasting with the spherical model [38], where the potential depths are shallower for the positive-parity states ( $V^0 \sim 40 \text{ MeV}$ ) and deeper for the negative-parity states ( $V^0 \sim 60 \text{ MeV}$ ). This improvement can be understood from the singleparticle energy in the Nilsson model. With deformation, the  $[101 \ 3/2]$  Nilsson state increases in energy for the positive-parity states (requiring a deeper potential to obtain the same eigenenergy), while the [220 1/2] Nilsson state decreases for negative-parity states (requiring a shallower potential to achieve the same eigenenergy).

Next, we compare the eigenphases calculated with Model I (std-PRM) and Model III (def-PF). Figure 4 illustrates the eigenphases for the (a)  $J^{\pi}=2^+$ , (b)  $J^{\pi}=1^+$ , and (c)  $J^{\pi}=3^+$  states. The solid and dotted lines represent the def-PF model and the std-PRM, respectively. Unlike the phase shifts for  $J^{\pi}=0^+$ ,  $1^-$ , and  $2^-$  depicted in Fig. 3,  $V_{\rm PF}$  alters the resonant energies and widths. Furthermore, for the  $3^+$  state in the std-PRM [dotted line in Fig. 4(c)], an additional resonance emerges at around  $\varepsilon \sim 1.6$  MeV, which can be regarded as the PF state. This resonance cannot be eliminated by changing  $V_{\rm def}^0$  if the neighboring  $3^+$  resonant state is correctly positioned. For comparison, the NCSM/RGM

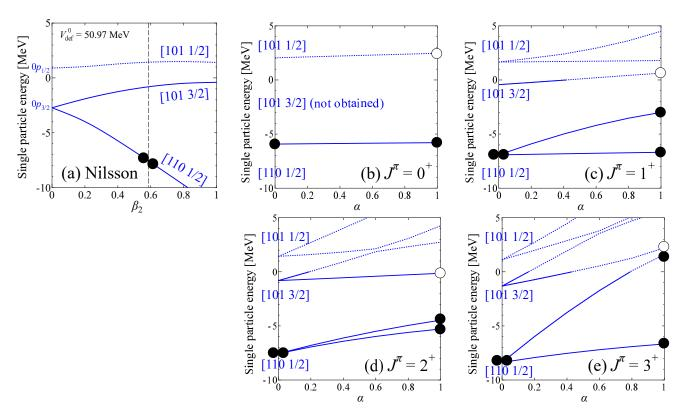


FIG. 2. Single particle energy used to define the forbidden states within the PRM framework. Panel (a) displays the Nilsson diagram, where the [110 1/2] Nilsson orbital is occupied by two protons, represented by the filled circles. The value  $\beta_2 = 0.586$  is indicated by the dashed line. Panels (b) to (e) illustrate the energy splitting as  $\alpha$  varies from 0 (Nilsson) to 1 (std-PRM) for the  $J^{\pi} = 0^+$  to  $3^+$  states, respectively, with  $\beta_2 = 0.586$ . Note that the potential depths of  $V_{\text{def}}$  are optimized for each  $J^{\pi}$  as summarized in Table I.

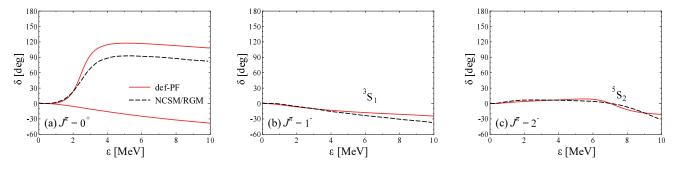


FIG. 3. Eigenphase shift for  $J^{\pi}=0^+$ , and diagonal phase shifts for  $J^{\pi}=1^-$  and  $2^-$  in the channel-spin representation. The solid line represents Model III (def-PF), while the dashed line corresponds to the ab initio NCSM/RGM calculation [10]. It should be noted that Model I (std-PRM) aligns with the solid line for these  $J^{\pi}$ .

calculations [10] are are also shown by the dashed lines. It should be noted that the potential depths are adjusted to the experimental ground and resonant energies in our calculations (both std-PRM and def-PF), whereas no phenomenological correction have been applied in the NCSM/RGM. For the resonances with a narrow width  $(J^{\pi} = 1^{+} \text{ and } 3^{+})$ , the observed behaviors are almost identical. However, for the resonances with a broader width, the present models do not exhibit the similar behavior regardless of the inclusion of  $V_{\rm PF}$ .

# B. Application to the $p + {}^{7}\mathrm{Be}$ reaction

As a test of the developed models, we have computed excitation functions for the elastic and inelastic cross sections for the  $p+{}^{7}$ Be reaction, and compared with the existing experimental data [43]. Figure 5 shows the excitation function of the  $p+{}^{7}$ Be elastic scattering cross section at 123°. Panel (a) compares three models, while panel (b) illustrates the  $J^{\pi}$  contributions by expanding the model space for our best result, the def-PF model. In panel (a), the dotted and solid lines represent the results

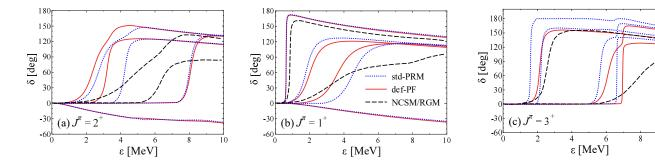


FIG. 4. Eigenphase shifts for  $J^{\pi} = 2^+$ ,  $1^+$ , and  $3^+$ . The line styles are the same as those used in Fig. 3, except that the std-PRM is additionally represented by the dotted line.

TABLE I. Potential depth parameters,  $V_{\text{def}}^{0}$  in MeV, used in the calculations. For Model II (sph-PF model), the parameters are identical to those used in Model III (def-PF model).

$I^{\pi}$	Model I	Model III
J	(std-PRM)	(def-PF)
$0_{+}$	48.00	48.00
$1^+$	49.83	48.70
$2^{+}$	50.97	50.41
$3^{+}$	52.41	49.98
$1^-$	48.00	48.00
$2^{-}$	53.00	53.00

of the PRM and def-PF model, respectively. Both models exhibit similar behavior in the low-energy region ( $\varepsilon \lesssim 1.3$  MeV) and predict the  $1_1^+$  resonance at  $\varepsilon = 0.63$  MeV, in agreement with the experimental data [43]. Above this energy region, the def-PF model well reproduces the second peak, mainly attributed to the  $3^+$  resonance at  $\varepsilon = 2.18$  MeV. On the contrary, as discussed in Fig 4, the PRM predicts an additional peak at around  $\varepsilon \sim 1.6$  MeV, which is inconsistent with the data. For comparison, the sph-PF model is shown by the dashed line. This result does not describes the experimental data even in the low-energy region, which cannot be solved merely by changing  $V_{\rm def}^0$ . These results underscore the importance of excluding Nilsson states as PF states to precisely describe deformed halo nuclei.

Finally, we apply the same model to inelastic scattering. Figure 6 presents the excitation function for p+7Be inelastic scattering cross section at 119°; the line styles are the same as those used in Fig. 5. In panel (a), although the peak structure of the def-PF model (solid line) more closely approaches the experimental peak at around  $\varepsilon=2.2$  MeV than the PRM (dotted line) [see also the phase shift in Fig. 4(a)], our def-PF model does not adequately reproduce the experimental data. In panel (b), the result of the def-PF model is further decomposed into each  $J^{\pi}$  component. The decomposition reveals that the inelastic peak is mainly composed of the  $2_3^+$  state at  $\varepsilon\sim3.2$  MeV, which is characterized by the large core-excited component  $[\mathcal{Y}_{p3/2}\otimes\phi_{1/2}]$ . Although the  $2^+$  state

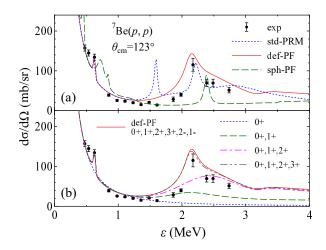


FIG. 5. Excitation function of  $p+{}^{7}\mathrm{Be}$  elastic scattering cross section at 123°. In panel (a), three models are compared: std-PRM (dotted line), def-PF model (solid line), and sph-PF model (dashed line). In panel (b), the  $J^{\pi}$  contributions are illustrated by expanding the model space for the def-PF model (our best result). The experimental data are taken from Ref. [43].

could be the key to understand the behavior of inelastic scattering, further refinements of the model are required to accurately understand the complex dynamics. To preserve the simplicity of the model, we have not attempted such modifications.

### IV. SUMMARY

In this study, we investigate various methods for excluding PF states in the PRM framework and evaluate their impact on the resonant-state properties. Previous studies [27, 28] introduced a simple technique for eliminating PF states in deformed halo nuclei by removing them after solving the Schrödinger equation. Despite its widespread application, our analysis reveals its limitation for  $^8\mathrm{B} = ^7\mathrm{Be} + p$ , where a PF state emerges as a resonant state. To overcome this limitation, we utilize Nilsson states as PF states in the OCM, allowing us to project

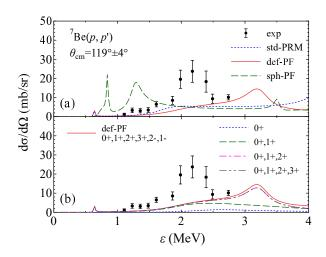


FIG. 6. Same as Fig 5, but for  $p+^{7}$ Be inelastic scattering cross section at 119°. The experimental data are from Ref. [43].

them out before solving the Schrödinger equation. This approach successfully reproduces the experimental data on elastic scattering excitation function, demonstrating its effectiveness. The same calculation predicts the presence of a low-energy bump in the inelastic scattering excitation function, although its position is overestimated by about 1 MeV. This result points out the need for further refinement of this model. This new approach not only overcomes the challenges encountered in  $^8{\rm B}$  calculations but also broadens the applicability to other deformed halo nuclei, such as  $^{17,19}{\rm C}$  or  $^{31}{\rm Ne}$ . The straightforward integration of this refined projectile wave function with CDCC and other reaction frameworks promises to open avenues for future research.

### ACKNOWLEDGMENTS

We are grateful to P. Punta for providing the benchmark results. One of the authors, S.W., thanks the faculty and staff at Universidad de Sevilla for their hospitality during his sabbatical stay, which enabled the completion of this work. S.W. is supported by JSPS KAKENHI Grant Number JP22K14043. A.M.M. is supported by MCIN/AEI/10.13039/501100011033, grant No. PID2020-114687GB-I00.

- [1] T. Nakamura, N. Kobayashi, Y. Kondo, Y. Satou, N. Aoi, H. Baba, S. Deguchi, N. Fukuda, J. Gibelin, N. Inabe, M. Ishihara, D. Kameda, Y. Kawada, T. Kubo, K. Kusaka, A. Mengoni, T. Motobayashi, T. Ohnishi, M. Ohtake, N. A. Orr, H. Otsu, T. Otsuka, A. Saito, H. Sakurai, S. Shimoura, T. Sumikama, H. Takeda, E. Takeshita, M. Takechi, S. Takeuchi, K. Tanaka, K. N. Tanaka, N. Tanaka, Y. Togano, Y. Utsuno, K. Yoneda, A. Yoshida, and K. Yoshida, Phys. Rev. Lett. 103, 262501 (2009).
- [2] T. Nakamura, N. Kobayashi, Y. Kondo, Y. Satou, J. A. Tostevin, Y. Utsuno, N. Aoi, H. Baba, N. Fukuda, J. Gibelin, N. Inabe, M. Ishihara, D. Kameda, T. Kubo, T. Motobayashi, T. Ohnishi, N. A. Orr, H. Otsu, T. Otsuka, H. Sakurai, T. Sumikama, H. Takeda, E. Takeshita, M. Takechi, S. Takeuchi, Y. Togano, and K. Yoneda, Phys. Rev. Lett. 112, 142501 (2014).
- [3] M. Takechi, T. Ohtsubo, M. Fukuda, D. Nishimura, T. Kuboki, T. Suzuki, T. Yamaguchi, A. Ozawa, T. Moriguchi, H. Ooishi, D. Nagae, H. Suzuki, S. Suzuki, T. Izumikawa, T. Sumikama, M. Ishihara, H. Geissel, N. Aoi, R.-J. Chen, D.-Q. Fang, N. Fukuda, I. Hachiuma, N. Inabe, Y. Ishibashi, Y. Ito, D. Kameda, T. Kubo, K. Kusaka, M. Lantz, Y.-G. Ma, K. Matsuta, M. Mihara, Y. Miyashita, S. Momota, K. Namihira, M. Nagashima, Y. Ohkuma, T. Ohnishi, M. Ohtake, K. Ogawa, H. Sakurai, Y. Shimbara, T. Suda, H. Takeda, S. Takeuchi, K. Tanaka, R. Watanabe, M. Winkler, Y. Yanagisawa, Y. Yasuda, K. Yoshinaga, A. Yoshida, and K. Yoshida, Phys. Lett. B 707, 357 (2012).
- [4] N. Kobayashi, T. Nakamura, Y. Kondo, J. A. Tostevin, Y. Utsuno, N. Aoi, H. Baba, R. Barthelemy, M. A. Famiano, N. Fukuda, N. Inabe, M. Ishihara, R. Kanungo, S. Kim, T. Kubo, G. S. Lee, H. S. Lee, M. Matsushita,

- T. Motobayashi, T. Ohnishi, N. A. Orr, H. Otsu, T. Otsuka, T. Sako, H. Sakurai, Y. Satou, T. Sumikama, H. Takeda, S. Takeuchi, R. Tanaka, Y. Togano, and K. Yoneda, Phys. Rev. Lett. **112**, 242501 (2014).
- [5] M. Takechi, S. Suzuki, D. Nishimura, M. Fukuda, T. Ohtsubo, M. Nagashima, T. Suzuki, T. Yamaguchi, A. Ozawa, T. Moriguchi, H. Ohishi, T. Sumikama, H. Geissel, N. Aoi, R.-J. Chen, D.-Q. Fang, N. Fukuda, S. Fukuoka, H. Furuki, N. Inabe, Y. Ishibashi, T. Itoh, T. Izumikawa, D. Kameda, T. Kubo, M. Lantz, C. S. Lee, Y.-G. Ma, K. Matsuta, M. Mihara, S. Momota, D. Nagae, R. Nishikiori, T. Niwa, T. Ohnishi, K. Okumura, M. Ohtake, T. Ogura, H. Sakurai, K. Sato, Y. Shimbara, H. Suzuki, H. Takeda, S. Takeuchi, K. Tanaka, M. Tanaka, H. Uenishi, M. Winkler, Y. Yanagisawa, S. Watanabe, K. Minomo, S. Tagami, M. Shimada, M. Kimura, T. Matsumoto, Y. R. Shimizu, and M. Yahiro, Phys. Rev. C 90, 061305 (2014).
- [6] P. Navrátil, R. Roth, and S. Quaglioni, Phys. Lett. B 704, 379 (2011).
- [7] K. Minomo, T. Sumi, M. Kimura, K. Ogata, Y. R. Shimizu, and M. Yahiro, Phys. Rev. Lett. 108, 052503 (2012).
- [8] S. Watanabe, K. Minomo, M. Shimada, S. Tagami, M. Kimura, M. Takechi, M. Fukuda, D. Nishimura, T. Suzuki, T. Matsumoto, Y. R. Shimizu, and M. Yahiro, Phys. Rev. C 89, 044610 (2014).
- [9] H. Kasuya and K. Yoshida, Prog. Theor. Exp. Phys. 2021, 013D01 (2020).
- [10] K. Kravvaris, P. Navrátil, S. Quaglioni, C. Hebborn, and G. Hupin, Phys. Lett. B 845, 138156 (2023).
- [11] R. Takatsu, Y. Suzuki, W. Horiuchi, and M. Kimura, Phys. Rev. C 107, 024314 (2023).

- [12] M. Kamimura, M. Yahiro, Y. Iseri, Y. Sakuragi, H. Kameyama, and M. Kawai, Prog. Theor. Phys. Suppl. 89, 1 (1986).
- [13] N. Austern, Y. Iseri, M. Kamimura, M. Kawai, G. Rawitscher, and M. Yahiro, Phys. Rep. 154, 125 (1987).
- [14] M. Yahiro, K. Ogata, T. Matsumoto, and K. Minomo, Prog. Theor. Exp. Phys. 2012, 01A206 (2012).
- [15] K. Hagino, K. Ogata, and A. Moro, Prog. Part. Nucl. Phys. 125, 103951 (2022).
- [16] N. C. Summers, F. M. Nunes, and I. J. Thompson, Phys. Rev. C 74, 014606 (2006).
- [17] N. C. Summers, F. M. Nunes, and I. J. Thompson, Phys. Rev. C 89, 069901 (2014).
- [18] R. de Diego, J. M. Arias, J. A. Lay, and A. M. Moro, Phys. Rev. C 89, 064609 (2014).
- [19] J. A. Lay, R. de Diego, R. Crespo, A. M. Moro, J. M. Arias, and R. C. Johnson, Phys. Rev. C 94, 021602 (2016).
- [20] R. de Diego, R. Crespo, and A. M. Moro, Phys. Rev. C 95, 044611 (2017).
- [21] R. Crespo, A. Deltuva, and A. M. Moro, Phys. Rev. C 83, 044622 (2011).
- [22] A. M. Moro and R. Crespo, Phys. Rev. C 85, 054613 (2012).
- [23] A. M. Moro and J. A. Lay, Phys. Rev. Lett. 109, 232502 (2012).
- [24] S. G. Nilsson, Dan. Mat. Fys. Medd. 29, 1 (1955).
- [25] I. Ragnarsson and S. G. Nilsson, Shapes and Shells in Nuclear Structure (Cambridge University Press, 1995).
- [26] A. Bohr and B. R. Mottelson, *Nuclear Structure* (World Scientific, Singapore, 1998).
- [27] Y. Urata, K. Hagino, and H. Sagawa, Phys. Rev. C 83, 041303 (2011).
- [28] Y. Urata, K. Hagino, and H. Sagawa, Phys. Rev. C 86, 044613 (2012).
- [29] A. Deltuva, A. Ross, E. Norvaišas, and F. M. Nunes, Phys. Rev. C 94, 044613 (2016).

- [30] S. Watanabe, K. Ogata, and T. Matsumoto, Phys. Rev. C 103, L031601 (2021).
- [31] P. Punta, J. A. Lay, and A. M. Moro, Phys. Rev. C 108, 024613 (2023).
- [32] S. Saito, Prog. Theor. Phys. 40, 893 (1968).
- [33] S. Saito, Prog. Theor. Phys. 41, 705 (1969).
- [34] H. Horiuchi, Prog. Theor. Phys. Suppl. **62**, 90 (1977).
- [35] R. C. Johnson and P. J. R. Soper, Phys. Rev. C 1, 976 (1970).
- [36] P. Descouvemont, Comput. Phys. Commun. 200, 199 (2016).
- [37] P. Descouvement and D. Baye, Rep. Prog. Phys. **73**, 036301 (2010).
- [38] R. Spartà, A. Di Pietro, P. Figuera, O. Tengblad, A. Moro, I. Martel, J. Fernández-García, J. Lei, L. Acosta, M. Borge, G. Bruni, J. Cederkäll, T. Davinson, J. Ovejas, L. Fraile, D. Galaviz, J. Halkjaer Jensen, B. Jonson, M. La Cognata, A. Perea, A. Sánchez-Benítez, N. Soić, and S. Viñals, Phys. Lett. B 820, 136477 (2021).
- [39] P. Maris, M. A. Caprio, and J. P. Vary, Phys. Rev. C 91, 014310 (2015).
- [40] P. Maris, M. A. Caprio, and J. P. Vary, Phys. Rev. C 99, 029902 (2019).
- [41] J. Aguilar and J. M. Combes, Commun. Math. Phys. 22, 269 (1971).
- [42] S. Aoyama, T. Myo, K. Katō, and K. Ikeda, Prog. Theor. Phys. 116, 1 (2006).
- [43] S. N. Paneru, C. R. Brune, R. Giri, R. J. Livesay, U. Greife, J. C. Blackmon, D. W. Bardayan, K. A. Chipps, B. Davids, D. S. Connolly, K. Y. Chae, A. E. Champagne, C. Deibel, K. L. Jones, M. S. Johnson, R. L. Kozub, Z. Ma, C. D. Nesaraja, S. D. Pain, F. Sarazin, J. F. Shriner, D. W. Stracener, M. S. Smith, J. S. Thomas, D. W. Visser, and C. Wrede, Phys. Rev. C 99, 045807 (2019).